JACS
JOURNAL OF THE AMERICAN CHEMICAL SOCIETY
Article
pubs.acs.org/JACS

Role of Subsurface Diffusion and Ostwald Ripening in Catalyst Formation for Single-Walled Carbon Nanotube Forest Growth

Shunsuke Sakurai,[†] Hidekazu Nishino,[†] Don N. Futaba,[†] Satoshi Yasuda,[†] Takeo Yamada,[†] Alan Maigne,[‡,§] Yutaka Matsuo,[⊥] Eiichi Nakamura,[⊥] Motoo Yumura,[†] and Kenji Hata*[,†,∥]

[†]Nanotube Research Center, National Institute of Advanced Industrial Science and Technology (AIST), Tsukuba 305-8565, Japan
[‡]Gatan Inc., 2-8-19 Fukagawa, Koto-ku, Tokyo 135-0033, Japan
[§]JST/SORST, c/o NEC, 34 Miyukigaoka, Tsukuba, Ibaraki 305-8501, Japan
[⊥]Department of Chemistry, The University of Tokyo, Hongo, Bunkyo-ku, Tokyo 113-0033, Japan
[∥]Japan Science and Technology Agency (JST), Kawaguchi 332-0012, Japan

Supporting Information

ABSTRACT: Here we show that essentially any Fe compounds spanning Fe salts, nanoparticles, and buckyferrocene could serve as catalysts for single-walled carbon nanotube (SWNT) forest growth when supported on AlO_x and annealed in hydrogen. This observation was explained by subsurface diffusion of Fe atoms into the AlO_x support induced by hydrogen annealing where most of the deposited Fe left the surface and the remaining Fe atoms reconfigured into small nanoparticles suitable for SWNT growth. Interestingly, the average diameters of the SWNTs grown from all iron compounds studied were nearly identical (2.8−3.1 nm). We interpret that the offsetting effects of Ostwald ripening and subsurface diffusion resulted in the ability to grow SWNT forests with similar average diameters regardless of the initial Fe catalyst.

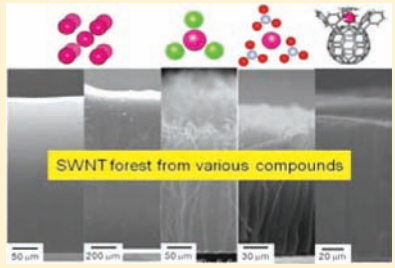

INTRODUCTION

Catalysts are one of the most important factors that govern the structure of a carbon nanotube (CNT). Carbon atoms catalytically decompose from carbon-containing molecules at the catalyst surface, dissolve into the catalyst bulk, and upon supersaturation precipitate as a carbon nanotube.[1] A similar synthetic mechanism has also been proposed for graphene formation and the Fischer−Tropsch synthesis of liquid fuels.[2,3] Intense effort has revealed that the structural features of CNTs, such as wall number, diameter, and chirality, are strongly correlated with the configuration and composition of the catalyst. For example, previous reports have shown that the diameter of the CNT is equivalent to the size of the catalyst nanoparticle.[4] The potential of catalysts to control the CNT structure is highlighted by the recent report of selective growth of both semiconductive and metallic single-wall carbon nanotubes.[5] In addition, recent progress has shown that numerous species, spanning from diamond to silica (SiO_2) can catalyze CNTs.[6] Nonetheless, iron remains the preferred choice for catalysts, particularly when high yield is desired, due to its ability to decompose hydrocarbon efficiently and the high solubility of carbon to form iron carbide.[7]

When SWNTs are synthesized in high yield on substrates, in most cases, the common factor is to use Fe as a catalyst on an AlO_x support layer. Development of this catalytic system has greatly advanced synthesis of single-walled carbon nanotubes (SWNTs) and has led to the realization of growth of dense, vertically aligned, and millimeter-long SWNTs (forests).[8−10] While other oxides, such as SiO_2 and TiO_2, have been successfully used as a support to grow multiwalled carbon nanotube (MWNT) forests, they do not appear to support aligned SWNT growth particularly for forests with height on the millimeter scale.[11] On the other hand, most approaches to grow millimeter-scale SWNT forests ranging from water-assisted method,[8] hot-filament technique,[9] and plasma-CVD,[10] all use Fe/AlO_x as a common catalyst system. SWNTs grown from Fe/AlO_x catalysts possess exceptional properties, such as high purity, high surface area, long length, and alignment. These properties have opened up new applications for CNTs, such as stretchable conductors,[12] supercapacitors,[13] and supertough fibers.[14] Synthesis of SWNT forests from Fe/AlO_x catalysts is a scalable process, as the large area (A4 size)[15] and continuous syntheses of SWNT forests have been demonstrated, and the first pilot plant is in operation that would enable industrial-scale mass production of economical SWNTs in the near future.

A common procedure to prepare the Fe/AlO_x catalyst begins from depositing a thin film of pure metal Fe by a dry process, such as sputtering, onto an AlO_x film. Subsequently, the Fe/AlO_x catalyst is exposed to hydrogen at high temperatures to break the Fe thin film into small catalytic nanoparticles. This preannealing process in hydrogen before growth, denoted as the "formation process," is crucial in preparing catalytic nanoparticles suited for SWNT growth. Although the importance has been empirically well-recognized,[16] very little

Received: September 15, 2011
Published: December 23, 2011

   dx.doi.org/10.1021/ja208706c | J. Am. Chem.Soc. 2012, 134, 2148−2153

research has been presented in the literature regarding the formation process. During the formation process, the AlO_x support plays a vital role in promoting the formation of nanoparticles to both increase their density beyond a level sufficient to achieve vertical alignment and restrict Fe surface migration necessary for nanoparticles suitable for SWNT growth.

In this article, we have studied the formation process of Fe/AlO_x catalyst for SWNT growth where we show that essentially any Fe compound could serve as a catalyst for SWNT forest growth when supported on AlO_x and annealed in hydrogen. This generality was explained by subsurface diffusion of Fe atoms into the AlO_x support invoked by hydrogen annealing. As a result, most of the deposited Fe leaves the surface and the remaining Fe reconfigures into small nanoparticles suited to grow SWNTs. Additionally, the average diameter of the SWNTs (and the size of Fe catalysts) grown from all iron compounds studied was nearly identical and fell within an unexpected narrow range of 2.8−3.1 nm. We propose that Ostwald ripening eliminated smaller nanoparticles while subsurface diffusion reduced the size of larger nanoparticles and resulted in a fairly uniform assembly of small catalysts regardless the initial Fe compound.

EXPERIMENTAL SECTION

Procedures for SWNT forest growth from a variety of iron compounds is represented in Figure 1a. $FeCl_3$ (iron chloride) and $Fe(NO_3)_3$ (iron nitrate) were selected to represent standard metal compounds. $Fe(C_{60}Ph_5)Cp$ (buckyferrocene) and chemically prepared colloidal iron nanoparticles (average size of 3.2 nm) were chosen to demonstrate the generality of our approach. In short, buckyferrocene was synthesized by a reaction between a fullerene derivative, $C_{60}Ph_5H$, and an iron complex, $[CpFe(CO)_2]_2$,[17] and colloidal iron nanoparticles were obtained by thermal decomposition of $Fe(CO)_5$ in an octyl-ether solution under N_2 atmosphere.[18] Each iron compound was dissolved into organic solvents and spin-coated or bar-coated onto sputtered AlO_x (40 nm on SiO_2/Si substrate) to form a thin Fe compound layer. As a reference, pure iron thin film was also prepared by sputtering. These Fe compounds were introduced into the furnace and exposed to H_2/He (40%/60%) ambient at 750 °C as the formation process. Subsequently, CNTs were synthesized from these catalysts by water-assisted chemical vapor deposition (CVD) with C_2H_4 (10%, 10 min) and H_2O vapor of 100−150 ppm at 750 °C. SWNT forests were characterized by scanning electron microscope (SEM), transmission electron microscope (TEM), and Raman spectroscopy (λ = 532 nm). Catalyst nanoparticles were observed using atomic force microscope (AFM).

For microscopic elemental analysis on Fe/AlO_x catalyst, "Ball-CVD" samples were prepared by deposition of Fe/AlO_x thin films (1.5 nm/10 nm) onto 50 nm SiO_2 nanoballs (on a TEM grid).[19,20] The use of the nanoballs increased the likelihood to find catalyst by TEM and allowed for cross-sectional viewing angles. Dark-field imaging and electron energy loss spectroscopy (EELS) analysis were performed using a scanning TEM (STEM) Hitachi HD-2300 with Gatan ENFINA spectrometer. X-ray photoelectron spectroscopy (XPS) and secondary ion mass spectroscopy (SIMS) measurements were performed on Fe/AlO_x thin films (1.5 nm/50−100 nm) sputtered on Si substrate. XPS analyses were performed on PHI ESCA-5800 system. Fe depth profiles were obtained by back-side SIMS measurements with primary ions of 14.5 keV Cs^-.

RESULTS AND DISCUSSION

Structure of SWNT Forest Grown from Various Iron Compounds. Vertically aligned CNT forests grew from every catalyst regardless of iron compounds as shown in SEM images and photographs (Figures 1b−g). The heights of the SWNT

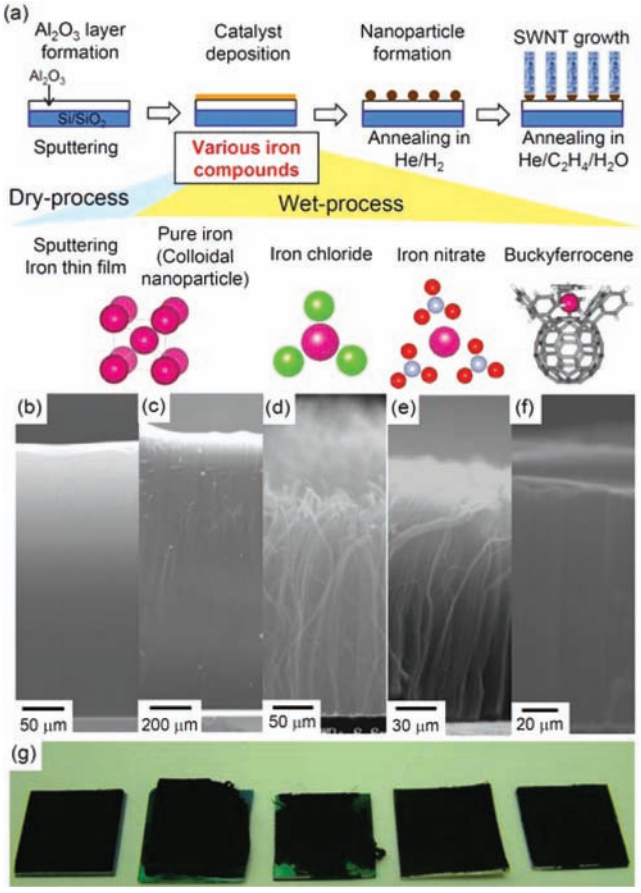

Figure 1. (a) Schematic representation of synthetic process for SWNT forest from various iron compounds. (b−f) SEM images of SWNT forests grown from (b) sputtered iron, (c) iron colloidal nanoparticles, (d) iron chloride, (e) iron nitrate, and (f) buckyferrocene. (g) Photographs of SWNT forest grown from various iron compounds.

forests (300 μm fo iron chloride, 200 μm for iron nitrate, and 150 μm for buckyferrocene) were within the same range of the SWNT forest grown from pure iron catalysts (400 μm for thin film and 1500 μm for nanoparticle). We would like to note that the synthesis of SWNT forests exceeding 100 μm from iron compound catalysts other than pure iron has not been previously reported. TEM observations confirmed that most of the CNTs were SWNTs.

Interestingly, regardless the Fe compound used as the catalyst, the average diameters of the SWNTs as estimated from size distribution histograms from TEM observations were nearly identical and fell within an unexpectedly narrow range of 2.8−3.1 nm (Figures 2a,b). The Raman spectra of SWNT forests (Supporting Information) grown from different iron compounds all showed identical characteristic radial breathing mode (RBM) peaks at 120 and 160 cm^{-1}, which showed good correspondence with the TEM analysis. In addition, the G-band (1590 cm^{-1}) to D-band (1340 cm^{-1}) intensity ratios were fairly similar, around 7, except SWNTs from iron chloride. The AFM images of the Fe/AlO_x after the formation process (H_2 ambient at 750 °C for 5 min) revealed a very similar surface configuration where a high density of small nanoparticles with somewhat uniform sizes were homogeneously distributed across the surface for all iron compounds. Specifically, the sizes of Fe catalyst nanoparticles as measured from the atomic force microscopy height profiles were in the range of 2−3 nm,

dx.doi.org/10.1021/ja208706c | J. Am. Chem.Soc. 2012, 134, 2148−2153

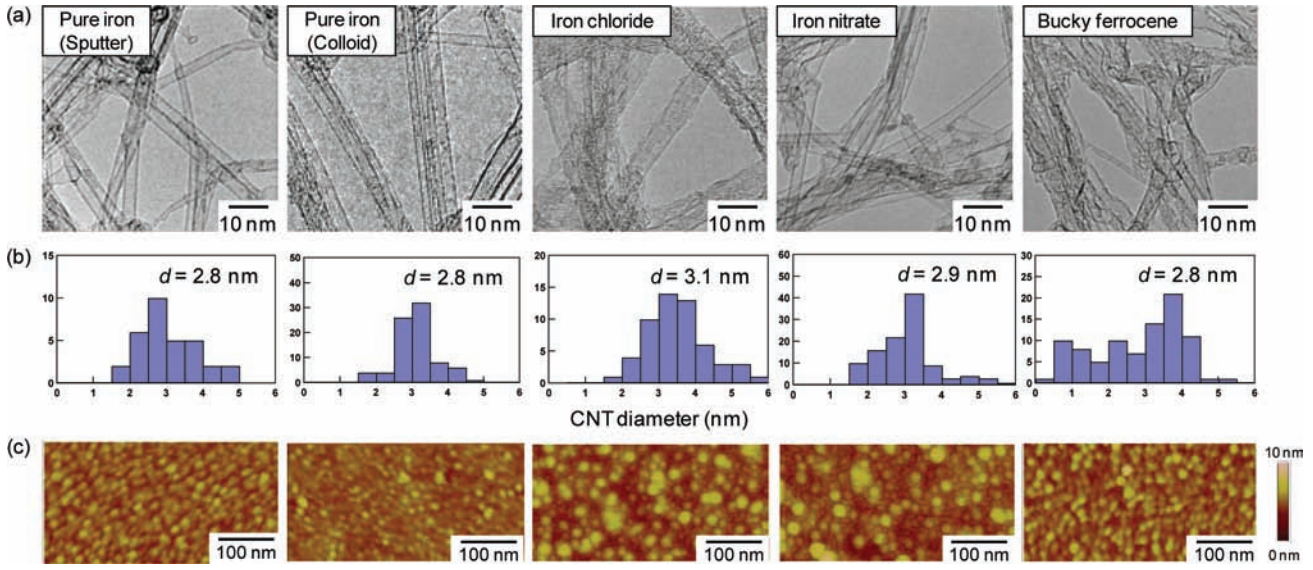

Figure 2. (a) TEM images of SWNTs grown from various catalysts. (b) Diameter distributions of SWNTs grown from various catalysts. (c) AFM images of iron nanoparticles formed after H_2 annealing.

regardless of the iron compound, and corresponded with the diameter of the grown SWNTs (Figure 2c). We would like to note that the iron particles obtained by thermolysis of buckyferrocene ($Fe(C_{60}Me_5)Cp$) alone at 700 °C were much larger (7.4 nm),[21] indicating the importance of the AlO_x support. One of the prominent features of the SWNTs grown from Fe/AlO_x was their relatively large diameter. We would like to note that other groups that have grown SWNT forests from Fe/AlO_x catalysts have also resulted in a similar average diameter of SWNT around 3 nm.[8,10,22] This average diameter is much larger than SWNTs made by laser ablation (1.4 nm),[23] arc-discharge (typically ~1.4 nm),[24] and the HiPco process (~1.1 nm)[25] and represents one of the unique features of the Fe/AlO_x catalyst. The observed generality in average diameter among different iron compounds indicates a common underlying mechanism as discussed in detail in the following.

Observation of Subsurface Diffusion of Fe Atoms into the AlO_x Support during the Formation Process. To gain insight into the catalyst formation mechanism of Fe/AlO_x catalysts when treated with hydrogen, we carried out both microscopic and macroscopic elemental analysis by STEM–EELS, XPS, and SIMS. Dark-field images and EELS analysis of the as-deposited "Ball-CVD" sample revealed the composition and configuration of the Fe/AlO_x catalyst system (Figure 3a,b). EELS spectra of the as-deposited Fe/AlO_x sample detected peaks from iron (Fe M peak at 53 eV), aluminum (Al L peak at 73 eV), and silicon (Si L peak at 100 eV). STEM–EELS mapping revealed three distinct layers, that is, a continuous thin film composed of Fe (green) and Al (blue) at the surface, a 10 nm Al layer beneath, and Si (red) nanoparticles at the center. The as deposited Fe/AlO_x sample was annealed in H_2/He ambient at 750 °C for 5 min as the formation process and then introduced in growth ambient (C_2H_4/H_2O/He, 1 min, at 750 °C) to demonstrate catalyst activity for CNT growth. Dark field images and STEM–EELS elemental maps showed the existence of Fe nanoparticles with size smaller than 5 nm protruding from the AlO_x layer surface and supporting CNT growth (Figure 3c,d). Importantly, the amount of Fe on the Fe/AlO_x sample had greatly reduced compared with the as-prepared sample, indicating subsurface diffusion of Fe atoms in the AlO_x

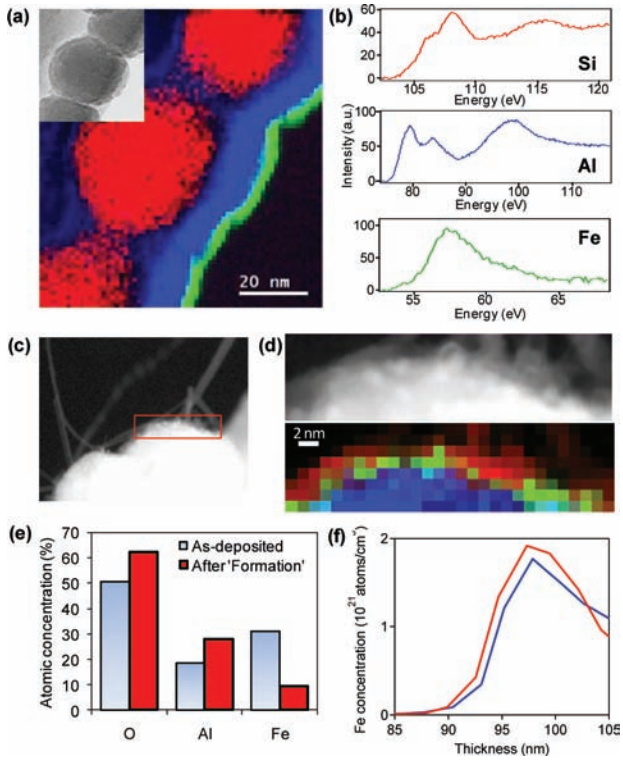

Figure 3. Elemental analyses by STEM–EELS, XPS, and SIMS. (a) STEM-EELS mapping images for "Ball-CVD" sample, where Si, Al, and Fe atoms are represented as red, blue, and greeen dots, respectively. Inset shows the corresponding TEM image. (b) Representative EELS spectra showing Si, Al, and Fe atoms. (c) Dark-field TEM image of CNT grown from Ball-CVD sample after 1 min exposure of C_2H_4. (d) EELS elemental mappings after 1 min exposure of C_2H_4, where blue, green, and red dots represent Al, Fe, and C atoms, respectively. (e) Atomic concentration analyzed by XPS measurement on the surface of Fe/Al_2O_3 thin film before and after He/H_2 annealing. (f) Fe depth profiles in Fe/AlO_x thin film before (blue) and after He/H_2 annealing (red). Profiles were obtained from the bottom sides of 100 nm AlO_x layer, using the back-side SIMS technique.

dx.doi.org/10.1021/ja208706c | J. Am. Chem.Soc. 2012, 134, 2148–2153

support during the formation process. When iron colloidal nanoparticles were treated with hydrogen, their size reduced as observed by AFM (Supporting Information), providing further evidence of subsurface diffusion of Fe atoms.

To provide macroscopic evidence of subsurface Fe diffusion, XPS and SIMS measurements were performed on as-deposited and hydrogen-annealed Fe/AlO_x thin films (1.5 nm/50−100 nm) on Si substrate. The atomic concentrations (Figure 3e) of Fe and Al estimated from XPS spectra (not shown) revealed a decrease of Fe concentration from 32% to 10% and an increase of Al concentration from 18% to 28% induced by the hydrogen annealing giving direct macroscopic evidence of Fe subsurface diffusion. Because the sampling depth of XPS is only several nanometers, the Fe concentration at the uppermost surface is expected to be even smaller. Indeed, the amount of Fe on the AlO_x support after the formation process was calculated as 0.087 nm from the product of the average volume of Fe nanoparticles (~14 nm^3 for spherical particle with 3 nm size) and the area density (6.2×10^{11} cm^{-2}).[26] This value represents only ~8.7% of the as-deposited Fe and thus means that most of the initially deposited Fe must have diffused into the AlO_x support and a small amount of Fe remained on the surface due to saturation of Fe atom concentration in the subsurface area of alumina. Amama et al. and Kim et al. have reported subsurface diffusion of Fe atoms into AlO_x support and have proposed this phenomenon to be the origin of growth termination.[27] Here, we have shown that the subsurface diffusion plays a critical role in forming a well-defined assembly of small Fe nanoparticles suited to grow SWNT forests. We estimated the average diffusion depth of Fe atoms as 2−3 nm, considering that XPS intensity (I) from atoms in depth of x is described as $I = \exp(-x/\lambda)$, where λ (ca. 3 nm) is the escape depth for the photoelectron. Additionally, we did not observe a clear difference in Fe depth profiles obtained by SIMS measurements before and after the formation process (Figure 3f). Since the resolution of the SIMS measurement is lower (ca. 10 nm) than that of XPS (<5 nm), this result indicates that subsurface diffusion is limited in the vicinity of the surface. We interpret that subsurface diffusion plays a key role in adjusting the Fe amount on the AlO_x support thus enabling synthesis of SWNT forests with similar sizes from various Fe compounds.

When the catalyst was subjected to the formation process without hydrogen (He ambient at 750 °C for 5 min), the as-deposited Fe formed into fewer nanoparticle catalysts, and CNT growth from these catalysts was not observed (Supporting Information). Although the importance of hydrogen annealing has been well recognized as reported by Hasegawa and Noda,[28] our results suggest hydrogen is indispensable to invoke subsurface diffusion and the formation of nanoparticles. How hydrogen reacts with the Fe films and forms the nanoparticles might be complicated with many processes involved. For example, it might be that hydrogen forms a disordered Al−Si−O mixed oxide, and iron diffusion is high in the mixed oxide. In addition, since the surface energy of metal Fe is higher than that of iron oxide,[29] reduced Fe atoms might easily react with the alumina support layer and diffuse into alumina. When SiO_2/Si support was used in place of the AlO_x support, a low density of iron nanoparticles with relatively large size (ca. 5 nm) were observed after the formation process (Supporting Information), demonstrating the importance of AlO_x support to achieve small and high density catalyst nanoparticles suited for SWNT growth.

Modeling Catalyst Nanoparticle Formation on the Al_2O_3 Support. Aligned SWNT forest growth demands strict fundamental requirements of the catalyst: (i) catalyst size control smaller than ~3 nm, (ii) catalyst density control where the average spacing among neighboring nanoparticles must be below ~20 nm, and (iii) catalyst stability at the growth temperature typically above 700 °C. The first requirement arises because of the empirically observed correlation between size and wall number, where nanoparticles larger than ~3 nm result in MWNTs, and the second requirement arises from the structural demand to support vertical growth. These fundamental requirements are not easily satisfied because Fe atoms migrate on the surface at high temperatures. This Fe surface migration would lead to morphological changes in the nanoparticles whereby larger particles grow in size at the expense of smaller particles, a phenomenon known as Ostwald ripening,[27,30] which has been reported to occur on AlO_x support layers where catalytic nanoparticles were observed to enlarge during CNT growth and eventually result in growth termination.[27]

The catalyst nanoparticle formation process was modeled on the basis of the interpretation that the balance between the two opposing processes (Ostwald ripening and subsurface diffusion) results in the condition that satisfies the fundamental requirements. The Fe catalyst particles were physically described as "bead" (analogous to a water bead) lying on the flat substrate with contact angle of θ, as schematically illustrated in Figure 4a. By Ostwald ripening, the growth of a particle with

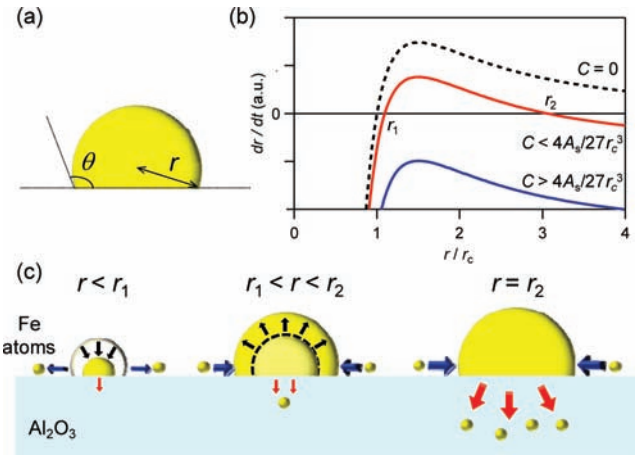

Figure 4. (a) The Fe nanoparticle modeled in eq 1. (b) dr/dt values versus r/r_c. (c) Schematic representation of the growth behavior of Fe nanoparticle.

radius of r is described as:

$$\frac{dr}{dt} = -\frac{A_s}{r^3}\left(1 - \frac{r}{r_c}\right) \quad (1)$$

,where A_s is constant and r_c is critical nucleus size (dotted line in Figure 4b).[30] It is important to note that nanoparticles cannot exist in the size range where dr/dt is negative. As shown in Figure 4b, according to this model, any particle with a size larger than r_c can exist stably, since the growth rate is positive up to infinite.

The effect of subsurface diffusion was incorporated into this equation as an additional term that decreases the growth rate as

dx.doi.org/10.1021/ja208706c | J. Am. Chem.Soc. 2012, 134, 2148−2153

$$\frac{dr}{dt} = -\frac{A_s}{r^3}\left(1 - \frac{r}{r_c}\right) - jS/(\partial n/\partial r) \quad (2)$$

,where j is the flux of subsurface diffusion into substrate, S is the vertical cross section of the nanoparticle bead, and n is the number of atoms in the nanoparticles. Substituting $n = 4\pi r^3\alpha/(3V_m)$, and $S = \pi(r \sin\theta)^2$, where $\alpha = (2 - 3\cos\theta + \cos^3\theta)/4$ and V_m is molar volume, into eq 2 gives

$$\frac{dr}{dt} = -\frac{A_s}{r^3}\left(1 - \frac{r}{r_c}\right) - C \quad (3)$$

,where $C = jV_m \sin^2\theta/(4\alpha)$.

The significant effect of introducing subsurface diffusion is that the growth rate is positive only in a specific range (between r_1 and r_2) provided $C < 4A_s/(27r_c^3)$ (see red line in Figure 4b). This is fully consistent with the experimental observation. According to this model, smaller particles with $r < r_1$ shrink and eventually extinguish due to the dissolution process of Ostwald ripening. Meanwhile, on the other end, the growth of the particles stops at $r = r_2$ because the effects of subsurface diffusion and Ostwald ripening are balanced (Figure 4c). When subsurface diffusion is strong ($C > 4A_s/(27r_c^3)$), dr/dt is always negative, and thus nanoparticles at any diameter cannot exist (blue line in Figure 4b). This model explains the experimentally observed results where SWNT forests grown from any Fe compound could result in SWNTs with similar average diameters. According to the model, we conclude that strict fundamental requirements of the catalyst Fe nanoparticle are achieved by the appropriate balance between two opposing mechanisms, Ostwald ripening and subsurface diffusion.

CONCLUSION

In conclusion, we demonstrate that essentially any Fe compound supported on AlO_x and treated with hydrogen could serve as a catalyst for SWNT forest growth. Interestingly, regardless of the Fe compound catalyst, the average diameters of the SWNTs were almost identical and fell within an unexpectedly narrow range of 2.8−3.1 nm. Analytical data from STEM−EELS, XPS, and SIMS suggest that an assembly of small iron nanoparticles with high density suited for SWNT forest growth was formed after hydrogen annealing. Experimental results and theoretical modeling demonstrate that Ostwald ripening and subsurface diffusion of Fe atoms into the AlO_x support were the two critical factors for the catalytic nanoparticle formation. Our model revealed that the resulting identical particle size was due to the appropriate balance between two opposing mechanisms. Our results suggest that controlling factors that influence Ostwald ripening and subsurface diffusion are promising approaches for further synthetic control of the catalyst size, size distribution, and density. From a practical side, our results imply that Fe compounds coated by wet-chemical processes could replace sputtered Fe metal films as catalysts for SWNT forests, opening up an economical and scalable catalyst preparation process for SWNT mass production.

ASSOCIATED CONTENT

Supporting Information

Additional AFM images of iron catalyst nanoparticles and Raman spectra of SWNTs grown from various iron compounds. This material is available free of charge via the Internet at http://pubs.acs.org.

AUTHOR INFORMATION

Corresponding Author

kenji-hata@aist.go.jp

ACKNOWLEDGMENTS

We wish to thank Mr. F. Kamada for assistance with experiments and discussion. This work is supported by MEXT (KAKENHI #22000008 to E.N.).

REFERENCES

(1) (a) Tessonnier, J.; Su, D. S. *ChemSusChem* **2011**, *4*, 824. (b) Yoshida, H.; Takeda, S.; Uchiyama, T.; Kohno, H.; Homma, Y. *Nano Lett.* **2008**, *8*, 2082.

(2) Li, X.; Cai, W.; Colombo, L.; Ruoff, R. S. *Nano Lett.* **2009**, *9*, 4268.

(3) (a) Chen, W.; Fan, Z.; Pan, X.; Bao, X. *J. Am. Chem. Soc.* **2008**, *130*, 9414. (b) E.; Koshino, M.; Saito, T.; Niimi, Y.; Suenaga, K.; Matsuo, Y. *J. Am. Chem. Soc.* **2011**, *133*, 14151.

(4) (a) Li, Y.; Kim, W.; Zhang, Y.; Rolandi, M.; Wang, D.; Dai, H. *J. Phys. Chem. B* **2001**, *105*, 11424. (b) Cheung, C. L.; Kurtz, A.; Park, H.; Lieber, C. M. *J. Phys. Chem. B* **2002**, *106*, 2429.

(5) (a) Harutyunyan, A. R.; Chen, G.; Paronyan, T. M.; Pigos, E. M.; Kuznetsov, O. A.; Hewaparakrama, K.; Kim, S. M.; Zakharov, D.; Sumanasekera, G. U.; Stach, E. A. *Science* **2009**, *326*, 116. (b) Chiang, W. H.; Sankaran, R. M. *Nat. Mater.* **2009**, *8*, 882. (c) Chiang, W. H.; Sakr, M.; Gao, X.; Sankaran, R. M. *ACS Nano* **2009**, *3*, 4023.

(6) (a) Yuan, D.; Ding, L.; Chu, H.; Feng, Y.; McNicholas, T. P.; Liu, J. *Nano Lett.* **2008**, *8*, 2576. (b) Huang, S.; Cai, Q.; Chen, J.; Qian, Y.; Zhang, L. *J. Am. Chem. Soc.* **2009**, *131*, 2094. (c) Takagi, D.; Kobayashi, Y.; Homma, Y. *J. Am. Chem. Soc.* **2009**, *131*, 6922. (d) Homma, Y.; Liu, H.; Takagi, D.; Kobayashi, Y. *Nano Res.* **2009**, *2*, 793.

(7) (a) Kong, J.; Cassell, A. M.; Dai, H. *Chem. Phys. Lett.* **1998**, *292*, 567. (b) Hernadi, K.; Fonseca, A.; Nagy, J. B.; Siska, A.; Kiricsi, I. *Appl. Catal., A* **2000**, *199*, 245. (c) Moisala, A.; Nasibulin, A. G.; Kauppinen, E. I. *J. Phys. (Paris)* **2003**, *15*, S3011. (d) Dupuis, A. C. *Prog. Mater. Sci.* **2005**, *50*, 929.

(8) (a) Hata, K.; Futaba, D. N.; Mizuno, K.; Namai, T.; Yumura, M.; Iijima, S. *Science* **2004**, *306*, 1362. (b) Chakrabarti, S.; Nagasaka, T.; Yoshikawa, Y.; Pan, L.; Nakayama, Y. *J. Jpn. Appl. Phys.* **2006**, *45*, L720. (c) Noda, S.; Hasegawa, K.; Sugime, H.; Kakehi, K.; Zhang, Z.; Maruyama, S.; Yamaguchi, Y. *J. Jpn. Appl. Phys.* **2007**, *46*, L399.

(9) (a) Xu, Y. Q.; Flor, E.; Kim, M. J.; Hamadani, B.; Schmidt, H.; Smalley, R. E.; Hauge, R. H. *J. Am. Chem. Soc.* **2006**, *128*, 6560. (b) Xu, Y. Q.; Flor, E.; Schmidt, H.; Smalley, R. E.; Hauge, R. H. *Appl. Phys. Lett.* **2006**, *89*, No. 123116.

(10) (a) Zhong, G.; Iwasaki, T.; Kawarada, H. *Carbon* **2006**, *44*, 2009. (b) Zhong, G.; Iwasaki, T.; Robertson, J.; Kawarada, H. *J. Phys. Chem. B* **2007**, *111*, 1907.

(11) (a) Fan, S.; Chapline, M. G.; Franklin, N. R.; Tombler, T. W.; Cassell, A. M.; Dai, H. *Science* **1999**, *283*, 512. (b) Esconjauregui, S.; Fouquet, M.; Bayer, B. C.; Eslava, S.; Khachadorian, S.; Hofmann, S.; Robertson., J. *J. Appl. Phys.* **2011**, *109*, No. 044303.

(12) Sekitani, T.; Nakajima, H.; Maeda, H.; Fukushima, T.; Aida, T.; Hata, K.; Someya, T. *Nat. Mater.* **2009**, *8*, 494.

(13) Izadi-Najafabadi, A.; Yasuda, S.; Kobashi, K.; Yamada, T.; Futaba, D. N.; Hatori, H.; Yumura, M.; Iijima, S.; Hata, K. *Adv. Mater.* **2010**, *22*, E235.

(14) Dalton, A. B.; Collins, S.; Muñoz, E.; Razal, J. M.; Ebron, V. H.; Ferraris, J. P.; Coleman, J. N.; Kim, B. G.; Baughman, R. H. *Nature* **2003**, *423*, 703.

(15) Yasuda, S.; Futaba, D. N.; Yamada, T.; Satou, J.; Shibuya, A.; Takai, H.; Arakawa, K.; Yumura, M.; Hata, K. *ACS Nano* **2009**, *3*, 4164.

(16) (a) Esconjauregui, S.; Bayer, B. C.; Fouquet, M.; Wirth, C. T.; Ducati, C.; Hofmann, S.; Robertson, J. *Appl. Phys. Lett.* **2009**, *95*, No. 173115. (b) Ago, H.; Ayagaki, T.; Ogawa, Y.; Tsuji, M. *J. Phys. Chem. C* **2011**, *115*, 13247. (c) Nessim, G. D.; Hart, A. J.; Kim, J. S.; Acquaviva, D.; Oh, J.; Morgan, C. D.; Seita, M.; Leib, J. S.; Thompson, C. V. *Nano Lett.* **2008**, *8*, 3587.
(17) (a) Sawamura, M.; Kuninobu, Y.; Toganoh, M.; Matsuo, Y.; Yamanaka, M.; Nakamura, E. *J. Am. Chem. Soc.* **2002**, *124*, 9354. (b) Herber, R. H.; Nowik, I.; Matsuo, Y.; Toganoh, M.; Kuninobu, Y.; Nakamura, E. *Inorg. Chem.* **2005**, *44*, 5629.
(18) Nishino, H.; Yasuda, S.; Namai, T.; Futaba, D. N.; Yamada, T.; Yumura, M.; Iijima, S.; Hata, K. *J. Phys. Chem. C* **2007**, *111*, 17961.
(19) Yamada, T.; Maigne, A.; Yudasaka, M.; Mizuno, K.; Futaba, D. N.; Yumura, M.; Iijima, S.; Hata, K. *Nano Lett.* **2008**, *8*, 4288.
(20) Zhu, H.; Suenaga, K.; Hashimoto, A.; Urita, K.; Hata, K.; Iijima, S. *Small* **2005**, *12*, 1180.
(21) Nakae, T.; Matsuo, Y.; Takagi, M.; Sato, Y.; Suenaga, K.; Nakamura, E. *Chem.—Asian J.* **2009**, *4*, 457.
(22) (a) Kayastha, V. K.; Wu, S.; Moscatello, J.; Yap, Y. K. *J. Phys. Chem. C* **2007**, *111*, 10158. (b) Mattevi, C.; Wirth, C. T.; Hofmann, S.; Blume, R.; Cantoro, M.; Ducati, C.; Cepek, C.; Knop-Gericke, A.; Milne, S.; Castellarin-Cudia, C.; Dolafi, S.; Goldoni, A.; Schloegl, R.; Robertson, J. *J. Phys. Chem. C* **2008**, *112*, 12207. (c) Yoshikawa, N.; Asari, T.; Kishi, N.; Hayashi, S.; Sugai, T.; Shinohara, H. *Nanotechnology* **2008**, *19*, 245607. (d) Esconjauregui, S.; Fouquet, M.; Bayer, B. C.; Ducati, C.; Smajda, R.; Hofmann, S.; Robertson, J. *ACS Nano* **2010**, *4*, 7431.
(23) Thess, A.; Lee, R.; Nikolaev, P.; Dai, H.; Petit, P.; Robert, J.; Xu, C.; Lee, Y. H.; Kim, S. G.; Rinzler, A. G.; Colbert, D. T.; Scuseria, G. E.; Tomanek, D.; Fischer, J. E.; Smalley, R. E. *Science* **1996**, *273*, 483.
(24) (a) Journet, C.; Maser, W. K.; Bernier, P.; Loiseau, A.; Chapelle, M. L.; Lefrant, S.; Deniard, P.; Leek, R.; Fischer, J. E. *Nature* **1996**, *388*, 756. (b) Iijima, S.; Ichihashi, T. *Nature* **1993**, *363*, 603.
(25) Chiang, I. W.; Brinson, B. E.; Huang, A. Y.; Willis, P. A.; Bronikowski, M. J.; Margrave, J. L.; Smalley, R. E.; Hauge, R. H. *J. Phys. Chem. B* **2001**, *105*, 8297.
(26) Futaba, D. N.; Hata, K.; Namai, T.; Yamada, T.; Mizuno, K.; Hayamizu, Y.; Yumura, M.; Iijima, S. *J. Phys. Chem. B* **2006**, *110*, 8035.
(27) (a) Amama, P. B.; Pint, C. L.; McJilton, L.; Kim, S. M.; Stach, E. A.; Murray, P. T.; Hauge, R. H.; Maruyama, B. *Nano Lett.* **2009**, *9*, 44. (b) Kim, S. M.; Pint, C. L.; Amama, P. B.; Zakharov, D. N.; Hauge, R. H.; Maruyama, B.; Stach, E. A. *J. Phys. Chem. Lett.* **2010**, *1*, 918.
(28) (a) Hasegawa, K.; Noda, S. *ACS Nano* **2011**, *5*, 975. (b) Hasegawa, K.; Noda, S. *Carbon* **2011**, *49*, 4497.
(29) Halden, F. A.; Kingery, W. D. *J. Phys. Chem.* **1955**, *59*, 557.
(30) (a) Lifshitz, I. M.; Slezhov, V. V. *J. Phys. Chem. Solids* **1961**, *19*, 35. (b) Wagner, C. *Z. Electrochem.* **1961**, *65*, 581. (c) Chakraverty, B. K. *J. Phys. Chem. Solids* **1967**, *28*, 2401. (d) Baldan, A. *J. Mater. Sci.* **2002**, *37*, 2172.